



Genesis of Tropical Storm Eugene (2005) from Merging Vortices Associated with ITCZ Breakdowns. Part II: Roles of Vortex Merger and Ambient Potential Vorticity

CHANH Q. KIEU AND DA-LIN ZHANG

Department of Atmospheric and Oceanic Science, University of Maryland, College Park, College Park, Maryland

(Manuscript received 29 July 2008, in final form 8 December 2008)

ABSTRACT

In this study, the roles of merging midlevel mesoscale convective vortices (MCVs) and convectively generated potential vorticity (PV) patches embedded in the intertropical convergence zone (ITCZ) in determining tropical cyclogenesis are examined by calculating PV and absolute vorticity budgets with a cloud-resolving simulation of Tropical Storm Eugene (2005). Results show that the vortex merger occurs as the gradual capture of small-scale PV patches within a slow-drifting MCV by another fast-moving MCV, thus concentrating high PV near the merger's circulation center, with its peak amplitude located slightly above the melting level. The merging phase is characterized by sharp increases in surface heat fluxes, low-level convergence, latent heat release (and upward motion), lower tropospheric PV, surface pressure falls, and growth of cyclonic vorticity from the bottom upward. Melting and freezing appear to affect markedly the vertical structures of diabatic heating, convergence, absolute vorticity, and PV, as well the production of PV during the life cycle of Eugene. Results also show significant contributions of the horizontal vorticity to the magnitude of PV and its production within the storm.

The storm-scale PV budgets show that the above-mentioned amplification of PV results partly from the net internal dynamical forcing between the PV condensing and diabatic production and partly from the continuous lateral PV fluxes from the ITCZ. Without the latter, Eugene would likely be shorter lived after the merger under the influence of intense vertical shear and colder sea surface temperatures. The vorticity budget reveals that the storm-scale rotational growth occurs in the deep troposphere as a result of the increased flux convergence of absolute vorticity during the merging phase. Unlike the previously hypothesized downward growth associated with merging MCVs, the most rapid growth rate is found in the bottom layers of the merger because of the frictional convergence. It is concluded that tropical cyclogenesis from merging MCVs occurs from the bottom upward.

1. Introduction

Despite considerable progress in the forecasts of tropical cyclone (TC) track and intensity during the past few decades, tropical cyclone genesis (TCG), a process by which a weak atmospheric disturbance grows into a tropical storm (TS), still remains elusive, partly because of the lack of high-resolution observations at the very early stage of TCG and partly because of the deficiencies in current TC models. In general, there are numerous tropical disturbances of different scales, including easterly waves and midlevel mesoscale convective vortices

(MCVs), during the warm season, but only a small percentage of them could develop into TCs (e.g., McBride and Zehr 1981; Molinari et al. 2000; DeMaria et al. 2001). Many processes leading to TCG are well known but they still remain poorly understood. In particular, we are still searching for the mechanisms by which the surface circulations could be spun up to initiate the wind-induced surface heat exchange (WISHE) process (Emanuel 1987) as a route to hurricanes.

The bottom-up and top-down hypotheses have been proposed as two of the possible processes leading to TCG from midlevel MCVs that often develop in the stratiform region of mesoscale convective systems (MCSs; Zhang and Fritsch 1987; Bartels and Maddox 1991). Specifically, Zhang and Bao (1996a,b) find that an MCV provides the necessary quasi-balanced forcing for the initiation and organization of (parameterized)

Corresponding author address: Dr. Da-Lin Zhang, Department of Atmospheric and Oceanic Science, University of Maryland, College Park, College Park, MD 20742–2425.
E-mail: dalin@atmos.umd.edu

deep convection and for the initial concentration of the low-level cyclonic vorticity, and that it is deep convection that contributes to the amplification of the low-level cyclonic vorticity through stretching in the presence of intensifying flows. The associated absolute angular momentum is then advected upward by convective updrafts to intensify the cyclonic flows above (see Zhang et al. 2001). This bottom-up mechanism was later advanced by cloud-resolving studies of Hendricks et al. (2004) and Montgomery et al. (2006), in which the concept of convective “hot towers” proposed by Riehl and Malkus (1958) was extended to that of “vortical hot towers” (VHTs) due to the development of intense cyclonic vorticity in convective cores. In their bottom-up hypothesis, Montgomery and Enagonio (1998) consider TCG to be a result of the mean-eddy interaction, the so-called axisymmetrization. That is, a midlevel MCV provides necessary cyclonic background rotation at the low levels, and a set of vorticity anomalies associated with VHTs contribute to the acceleration of the mean vortex through merging with neighboring VHTs and subsequent axisymmetrization. Montgomery and Kallenbach (1997) show that axisymmetrization can spin up a mesoscale vortex even in a nondivergent barotropic model.

In contrast, the top-down hypotheses deal with two different scenarios: one is related to the merging dynamics of midlevel MCVs within a larger-scale low-level cyclonic background flow (Ritchie and Holland 1997; Simpson et al. 1997), whereas the other focuses more on the thermodynamics of a single MCV (Bister and Emanuel 1997). In the former case, the merger of midlevel MCVs accompanies the downward extension of cyclonic vorticity due to the increase of the penetration depth and horizontal vortex size, leading to the amplification of surface rotation. In the latter case, the top-down hypothesis relies on the evaporative cooling as a means to advect the midlevel MCV downward and then replace the anticyclonic circulation near the surface. TCG occurs as soon as the WISHE process is initiated.

A recent statistical study of TCG over the eastern Pacific during the active seasons of 1999–2003 shows that most of the TCG events in this ocean basin are associated with intertropical convergence zone (ITCZ) breakdowns caused by easterly propagating tropical disturbances (Wang and Magnusdottir 2006). Although the ITCZ breakdowns could be attributed to the internal dynamical instability—that is, the so-called roll-up mechanism discussed by Nieto Ferreira and Schubert (1997)—Wang and Magnusdottir’s study appears to suggest that merging MCVs associated with the ITCZ breakdowns may be more efficient in initiating the TCG processes and subsequently generating the mesoscale disturbances of tropical depression strength.

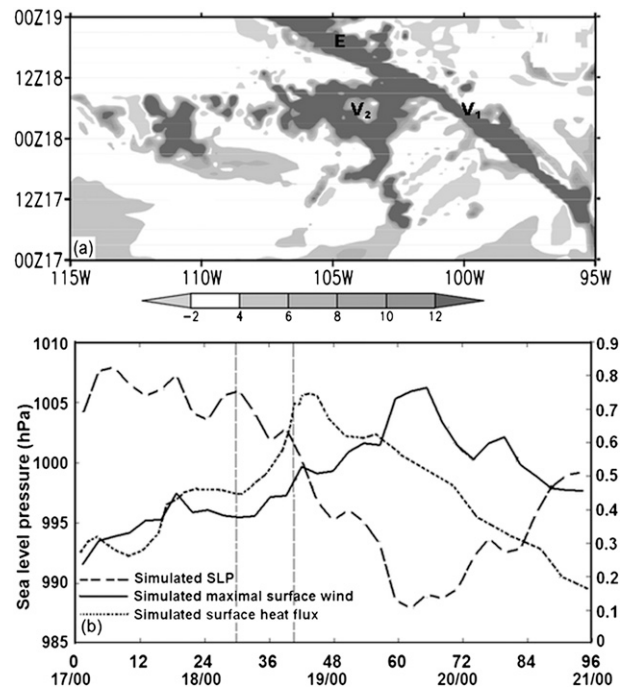


FIG. 1. (a) Hovmöller diagram of the vertical absolute vorticity (gray scale interval is shown in units of 10^{-5} s^{-1}) at 850 hPa over the longitudinal span of 115° – 95° W from the hourly model outputs during the first 2-day period of 17/00–00 to 19/00–48. It is meridionally averaged within a 1° width centered along V_1 initially and at Eugene after the merger. Here, V_1 and V_2 denote the two MCVs associated with the formation of TS Eugene (“E”). (b) Time series of the simulated maximum surface wind (solid; right ordinate in 50 m s^{-1}), minimum sea level pressure (dashed; left ordinate in hPa), and the $(720 \text{ km} \times 720 \text{ km})$ area-averaged surface heat fluxes (dotted; right ordinate in $5 \times 10^2 \text{ W m}^{-2}$) during the 4-day period of 17/00–00 to 21/00–96. Thin dashed lines denote the merging phase; similarly for the rest of figures.

In Kieu and Zhang (2008, hereafter Part I), we have presented the genesis of TS Eugene (2005), occurring during the National Aeronautics and Space Administration (NASA’s) field campaign of the Tropical Cloud Systems and Processes (TCSP; see Halverson et al. 2007), from merging MCVs associated with the ITCZ breakdowns using satellite data and observational analysis together with 4-day cloud-resolving simulation of its life cycle with the Advanced Research Weather Research and Forecasting model (WRF-ARW) at the finest grid size of 1.33 km (Part I). It is shown that the WRF model reproduces reasonably well the movements, intensities, coalescence, and capture of two midlevel MCVs (referred to as V_1 and V_2 ; see Fig. 1a) at 39 h into the integration as well as the subsequent track and intensification of the merger to TS Eugene in association with the poleward rollup of the ITCZ, as verified against available observations. Model results show that as the two MCVs are merged, deep convection intensifies and the

midlevel potential vorticity (PV) increases in amplitude and volume, thereby allowing the corresponding broad surface cyclonic circulations to merge into one surface mesolow and then amplify to TS intensity.

The objectives of the present study are (i) to examine the kinematics of the vortex merger in relation to convectively generated vortices (CGVs) in the ITCZ and the associated multiscale interactive processes; (ii) to quantify the roles of merging MCVs, surface heat fluxes, and PV sources in the ITCZ in the formation of TS Eugene (2005); and (iii) to determine whether or not TCG from merging MCVs would occur from the bottom upward or the top downward. These objectives will be achieved by analyzing the 4-day high-resolution simulation of TS Eugene (2005) through the PV and absolute vorticity budgets.

The next section presents the vortex merging kinematics in the context of PV and the time series of surface heat fluxes to facilitate the subsequent discussion of the roles of merging MCVs and CGVs in TCG. Section 3 describes the theoretical framework and examines the vortex merging dynamics and the effects of PV sources in the ITCZ on the development of Eugene through the analyses of PV budgets. Section 4 explores the possible mechanism by which the bottom-up or top-down growth of cyclonic vorticity is operative during the merging phase through the vertical absolute vorticity budgets. A summary and concluding remarks are given in the final section.

2. Vortex-merging kinematics

It is apparent from Figs. 1a and 1b that we may divide Eugene's life cycle into four phases: a pregenesis phase with a slow evolution of V_2 prior to 0600 UTC 18 July or 30 h into the simulation (hereafter 18/06–30; a vortex-merging spin-up phase from 18/06–30 to 18/15–39, a self-sustained deepening phase from 18/15–39 to 19/18–66, and a decaying phase afterward. In Part I, we have shown that the first two phases are characterized respectively by a loosely defined ITCZ surface trough with trade winds from both hemispheres and a mesolow with the maximum surface wind reaching 18 m s^{-1} —a threshold for a TS. The simulated maximum surface wind of 38 m s^{-1} at 19/18–66 just exceeds the threshold for a hurricane (Fig. 1b). In addition, we have briefly illustrated the interaction of the two midlevel MCVs during the vortex-merging phase. Of importance is that the area-averaged surface (sensible and latent) heat fluxes increase slowly prior to the merger but sharply ($>60\%$) during the merging phase (Fig. 1b), indicating that the merger helps initiate the WISHE processes for a self-sustained deepening phase. Note that despite the intensifying surface winds, the surface fluxes decrease rapidly shortly after the merger, owing to the storm's movement over a

colder ocean surface (cf. Fig. 6a in Part I and Fig. 1b here). As will be seen later, the storm could continue its deepening to hurricane intensity during the period of 18/20–44 to 19/18–66, mainly because of the continuous lateral PV fluxes from the ITCZ.

To help visualize the kinematics of the vortex merger, Fig. 2 shows the east–west vertical cross sections of the meridionally averaged PV and its local tendencies during the period of 18/09–33 and 18/23–47, encompassing the merger and its subsequent intensification. It is obvious that the two MCVs consist of many meso- γ scale PV patches or CGVs tilting cyclonically downshear with their PV centers located in the midtroposphere. These small-scale features have not been previously shown because of the use of coarse-resolution observations and simulations. These vortices appear to be the congregation of smaller-scale VHTs resulting partly from their mergers (Fig. 3) and partly from the meridional averaging. These convectively generated VHTs, as indicated by collocated updrafts and vorticity centers, begin to increase in coverage as V_1 approaches V_2 , and they become better organized around the MCVs (Fig. 3a), especially a deep layer mesolow associated with the merger (see Fig. 10 in Part I and Fig. 3b here). Because major convective developments in the ITCZ occur on the southern half of the MCVs' circulations prior to merger, most γ -scale vortices in V_2 are seen drifting cyclonically eastward (cf. Figs. 2 and 3), as also indicated by the PV tendencies occurring ahead of CGVs. The MCV merging processes are marked by the gradual capture of each of the γ -scale vortices within the slow-drifting V_2 by the northwestward fast-propagating V_1 and by the organized upward motion at increasingly larger scales, with the peak magnitudes in the upper troposphere (see Figs. 10 and 11 in Part I). Some patches of large positive PV tendencies are associated with both the advection and the diabatic generation of PV, as will be seen in the next section. Note that although the meridionally averaged vertical motion is upward near the merger's center, horizontal maps show little radar reflectivity (just like an "eye") over the central portion of the TC circulation (see Fig. 12 in Part I).

In general, the meridionally averaged PV traces reasonably well the evolution and interaction of CGVs and their merging into the PV volume of V_1 , leading to the genesis of Eugene, except for a few PV patches in V_2 (e.g., the leftmost one at 18/11–35) that appear to change sharply in magnitude with time because of the diabatic destruction of PV (not shown). Note that because of its smaller size, V_1 's circulations at individual levels are seen being absorbed by V_2 's as V_1 coalesces and enters the northern half portion of V_2 's circulation (see Fig. 6 in Part I and Fig. 3 here), so V_1 may

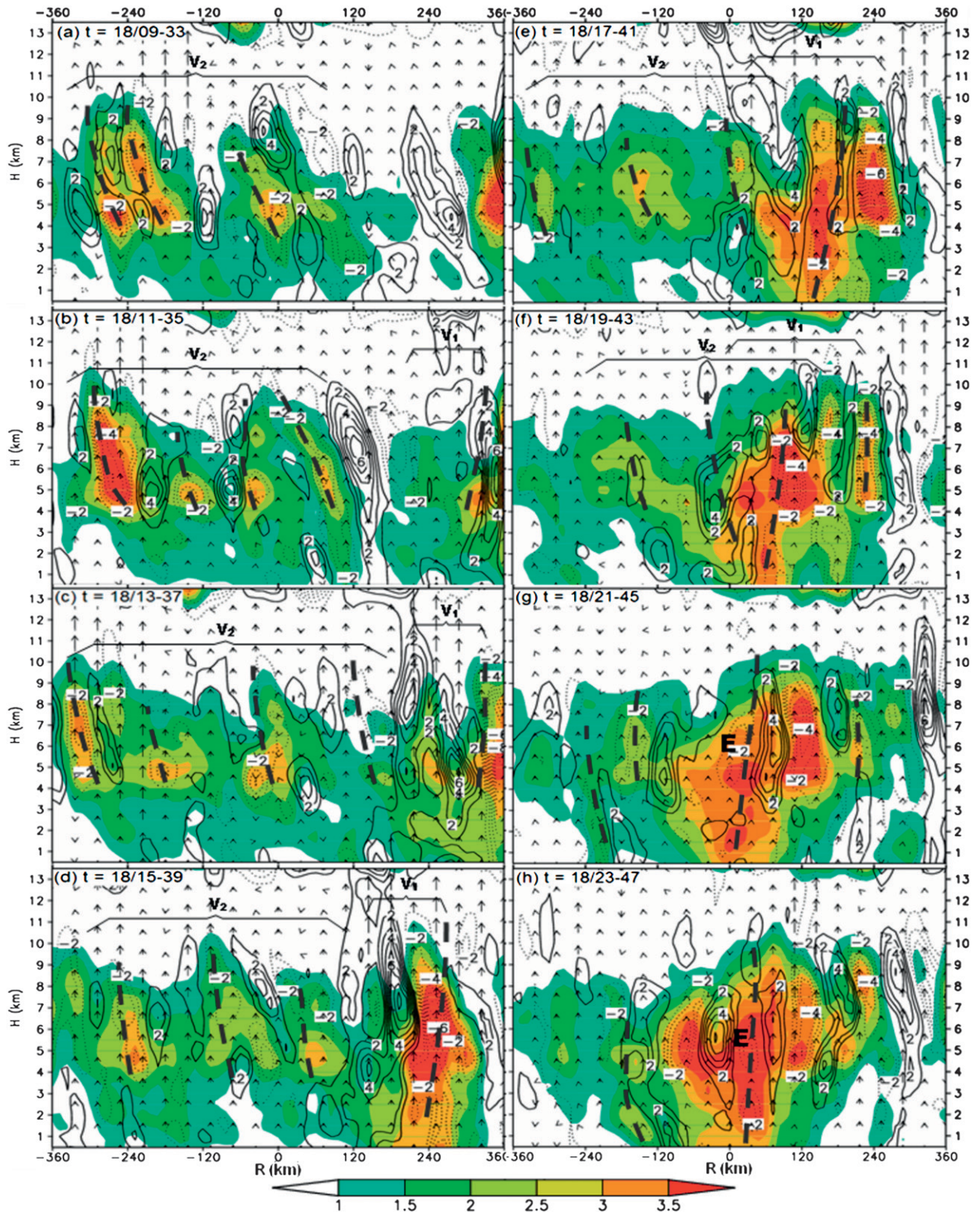


FIG. 2. Vertical cross sections of the north-south mass-weighted PV (shadings every 0.5 PVU, where $1 \text{ PVU} = 10^{-6} \text{ m}^2 \text{ s}^{-1} \text{ K kg}^{-1}$) within $\pm 360 \text{ km}$ along the line through the centers of V_1 and V_2 , and the corresponding PV tendency (contoured every $10^{-4} \text{ PVU s}^{-1}$), superimposed with the vertical motion vectors, during the period of 18/09-33 to 18/23-47. Bold dashed lines indicate convectively generated vortices spawned within V_2 and V_1 . Note that a vertical grid interval represents a vector scale of 1 m s^{-1} .

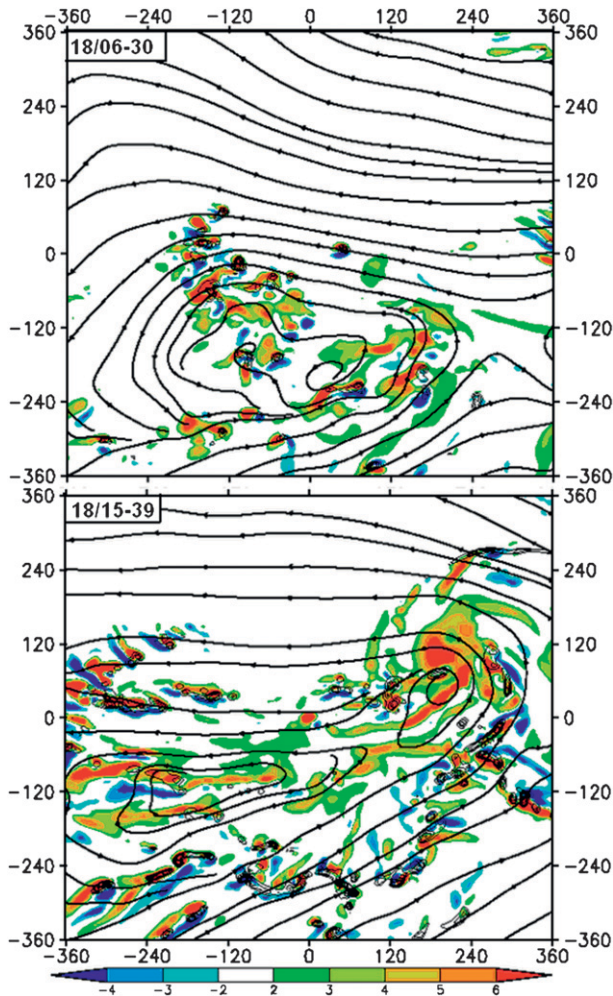


FIG. 3. Horizontal cross sections of the absolute vorticity (shaded every $2 \times 10^{-4} \text{ s}^{-1}$), and vertical motion (contoured every 0.5 m s^{-1}) at $z = 3 \text{ km}$, superimposed with the midlevel streamlines valid (top) at 18/06–30, before the merger, and (bottom) at 18/15–39, during the merger.

be viewed horizontally as a “comma head” that rolls up northwestward to congregate the PV-containing γ -vortices in V_2 (and later in the ITCZ) in the tail (Fig. 4).

Of importance to this study are significant increases in intensity and three-dimensional (3D) volume of PV as V_1 captures each γ -scale vortex or vorticity band after 18/15–39. The increases are especially pronounced in the midtroposphere where the peak PV associated with most of the γ -scale vortices is located. The lower-level PV also increases in magnitude and area coverage, which results mostly from the merging of the lower-level PV sources, as indicated by positive PV tendencies in the lower troposphere. This indicates that the vertical PV distribution of these γ -scale vortices may determine to some extent the corresponding vertical PV structures of TCs after being merged.

In addition to their effects on the vertical distribution of PV, the γ -scale vortices propagating cyclonically in the merger become more upright because of the development of strong upward motion after reaching TS intensity (e.g., at 18/23–47). By this time, a robust vortex merger emerges with higher PV values but a circulation size that is smaller than the earlier congregated V_1 and V_2 circulation; that is, the west–east width of the merger has shrunk by half the total width of V_1 and V_2 during the past 10 h (i.e., from 18/13–37 to 18/23–47). Note that the merger’s circulation size is much greater than the size of the individual V_1 or V_2 (see Fig. 4). Clearly, the shrunk total circulation size and the increased PV amplitude and high-PV volume associated with the vortex merger, caused essentially by latent heat release, are all favorable for the deepening of the surface cyclone (Fig. 1). It is evident that these 3D merging processes could not be adequately described by nondivergent barotropic models (e.g., Montgomery and Kallenbach 1997; Prieto et al. 2003).

Figure 4 shows that these γ -scale PV (or cyclonic vorticity) patches associated with V_2 are aligned along the mean sheared flows into linear PV bands. Of interest is that these convectively generated PV bands are the “feeder” of PV into V_1 as the comma head rolls up northwestward. Specifically, prior to merger (e.g., at 18/09–33), the dominant larger-scale flows are easterly and westerly on the respective northern and southern side of the ITCZ, with significant shear vorticity. As more PV bands are fed into in the comma head and locally concentrated in V_1 ’s circulation, more shear vorticity is converted to curvature vorticity (see Bell and Keyser 1993; Zhang and Bao 1996b), leading to the generation of an intensifying TC circulation with the weakest flow at its center. The associated TC circulation also increases in size and intensity with time as more PV patches are congregated. The complete merging of the two MCVs gives rise to the formation of Eugene after 18/21–45. Note the continued PV fluxes associated with deep convection in the westerly flows from the ITCZ into Eugene’s circulation, which (as will be seen in the next section) play an important role in increasing the high-PV volume near the circulation center and in facilitating the continued deepening of the storm regardless of the rapid decreases in surface heat fluxes.

3. Vortex-merging dynamics

We have seen from Figs. 2 and 4 the substantial concentration of PV near the merger’s circulation center and the increased high-PV volume during the merging phase. In this section, we attempt to quantify the dynamical processes accounting for the vortex-merging scenarios and the roles of CGVs embedded in the ITCZ in the genesis of TS Eugene through the PV budget analysis.

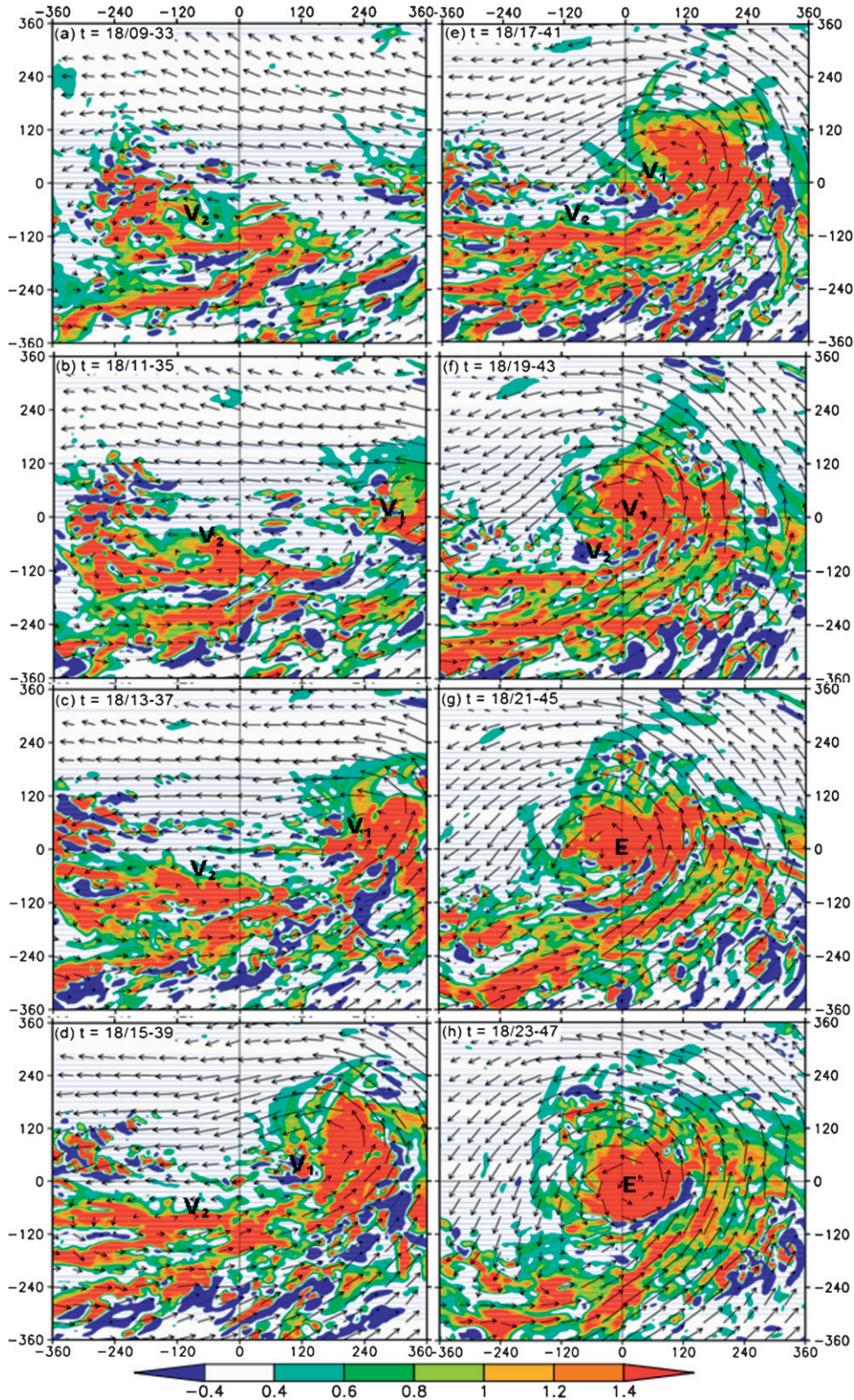


FIG. 4. As in Fig. 2, but for the horizontal distribution of the vertically mass-weighted PV (shadings every 0.2 PVU), superimposed with flow vectors at $z = 3$ km. Note that a grid interval represents the vector scale of 25 m s^{-1} .

a. Dynamical framework

In this study, we choose to examine the PV budgets in a quasi-Lagrangian framework following the storm. We start from the nonhydrostatic PV equation of Haynes and McIntyre (1987):

$$\frac{\partial q}{\partial t} = -\mathbf{u} \cdot \nabla q + \frac{1}{\rho} \nabla \cdot (H\boldsymbol{\omega} + \mathbf{F} \times \nabla \theta), \quad (1)$$

where \mathbf{u} is the 3D wind field, H is the 3D diabatic heating rate, and \mathbf{F} is the 3D frictional force. It is clear that diabatic heating and friction are the sources and sinks of PV in the troposphere. Although Eq. (1) is useful for estimating the spatial structures of PV budgets in TCs, it would be more appropriate to use the area- or volume-averaged PV budgets that could distinguish internal PV forcing processes from the boundary fluxes, especially when the *time evolution of the storm-scale integrated quantities in a storm-relative system* is examined. In the latter case, Eq. (1) has to be written as a volume-integration and then averaged by the control volume, hereafter referred to as bulk PV (BPV) following the storm; that is,

$$\begin{aligned} \frac{d}{dt} \left(\int_{V(t)} q dV \right) &= \int_{V(t)} \frac{\partial q}{\partial t} dV + \int_S q \mathbf{U} \cdot \mathbf{n} dS \\ &= - \int_{V(t)} (\mathbf{u} \cdot \nabla q) dV + \int_{V(t)} \frac{\nabla \cdot (H\boldsymbol{\omega})}{\rho} dV \\ &\quad + \int_{V(t)} \frac{\nabla \cdot (\mathbf{F} \times \nabla \theta)}{\rho} dV + \int_S q \mathbf{U} \cdot \mathbf{n} dS, \end{aligned} \quad (2)$$

where \mathbf{U} is the movement of the lateral boundaries. Similarly, the vertical profiles of the area-averaged PV (APV) budgets can be estimated by applying the area integration and then area-averaging to all the terms in Eq. (1). After reorganizing the first and last terms on the rhs and using $\nabla \cdot \boldsymbol{\omega} = 0$, Eq. (2) can be rewritten in a more meaningful form as

$$\begin{aligned} \frac{d}{dt} \left(\int_{V(t)} q dV \right) &= \int_{V(t)} (q \nabla \cdot \mathbf{u}) dV + \int_{V(t)} \frac{\boldsymbol{\omega} \cdot \nabla H}{\rho} dV \\ &\quad + \int_{V(t)} \frac{\nabla \cdot (\mathbf{F} \times \nabla \theta)}{\rho} dV \\ &\quad + \int_{S(t)} q (\mathbf{U} - \mathbf{u}) \cdot \mathbf{n} dS. \end{aligned} \quad (3)$$

Equation (3) states that the time rates of BPV changes (QTEN) are determined by the terms on its rhs, which are from left to right the condensing or diluting rates of BPV due to the 3D velocity divergence (3DIV;

QCON) [see the PV substance related discussion in Haynes and McIntyre (1987)], the diabatic PV production rates (QH), the divergence of $\mathbf{F} \times \nabla \theta$, and the net across-boundary PV fluxes (QBND) between the 3D normal-to-boundary flows (QFLX) and the control volume's movement (QMOV). One can see that unlike the differential form of PV Eq. (1), Eq. (3) has two additional forcing terms (i.e., QCON and QBND), which may change the total PV within a volume even in the absence of diabatic heating and frictional contribution. Note that because 3D divergence is proportional to minus the time rates of density changes (i.e., $-d \ln \rho / dt$), QCON is related ultimately to the mass exchange rate of the control volume with its surrounding environment. All the rhs terms are calculated with the hourly 4-km-resolution model output, including the heating rate H , and then averaged with the total volume [i.e., dividing by $V(t)$].

In this study, the control volume, following V_2 prior to merger and then Eugene after its formation, is defined with the top boundary at $z = 11.5$ km to minimize the impact of high PV in the stratosphere and the bottom boundary at $z = 1.5$ km, which is slightly above the PBL, to eliminate the PBL effects (i.e., $\mathbf{F} \times \nabla \theta$) on the PV budget calculations. Here we shall refer to all the *volume integrals* on the rhs of Eq. (3) as internal dynamical forcings because, unlike the *surface integrals*, they take into account all of the information within the control volume. It is evident that QCON and QH represent the internal sources–sinks of BPV in the absence of the PBL effects, whereas QBND denotes external sources–sinks of BPV. To make sure that the budget residues are small for the purpose of this study, we have compared the time rates of the BPV changes calculated from the lhs term of Eq. (3) (given in Fig. 6a) to those obtained by summing up all the rhs forcing terms during the 4-day integration and noticed that the differences between the two approaches are small (not shown). In the next section, we shall refer to Eqs. (1) and (3) as simply the PV budget and the BPV budget, respectively, and similarly for the vertical absolute vorticity budgets to be discussed in section 4.

It should be mentioned that the budget Eqs. (1) and (3) would differ drastically when written in isobaric or isentropic coordinates. That is, because of the use of hydrostatic approximation, only the vertical component of absolute vorticity is often considered in these coordinate systems. As will be seen in the next subsection, the horizontal components of relative vorticity turn out to be increasingly important in intensifying TCs because of the presence of large vertical wind shear associated with the TC tangential flow. Without the representation of horizontal vorticity, PV, defined as scalar multiplication

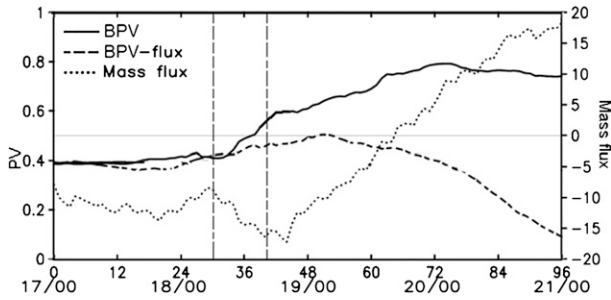


FIG. 5. Time series of the BPV (PVU) from the hourly model outputs: BPV (solid) and BPV after subtracting the net PV flux at the boundaries (short dashed) for a control volume of $720 \text{ km} \times 720 \text{ km} \times 10 \text{ km}$, following V_2 until 18/18–42 and thereafter Eugene. The corresponding total mass flux is also plotted (dotted; 10^7 kg s^{-1}).

of the 3D absolute vorticity vector and the 3D potential temperature gradient, might not be meaningful to the understanding of PV structures and evolution of TCs, especially to its conservative property. Thus, PV in height coordinates is used in the present study because it is treated most completely with both the vertical and horizontal components of absolute vorticity.

b. Bulk PV budget analysis

To see to what extent the PV equation can be used to characterize the vortex-merging processes and the role of CGVs in the ITCZ during the life cycle of Eugene, we consider first the time series of the BPV budget. Figure 5 shows that the BPV associated with V_2 increases slowly prior to merger (i.e., 18/06–30), moderately to sharply during its merging with V_1 (i.e., from 18/12–30 to 18/18–42), and steadily until Eugene reaches its maximum intensity at 19/18–66; shortly after, it slowly decreases. These sequences correspond reasonably well to the aforementioned four phases of Eugene’s life cycle (cf. Figs. 5 and 1b). Similar scenarios can also be seen from the time series of the BPV tendency (cf. Figs. 5 and 6a). The BPV doubles in magnitude (i.e., from 0.4 to 0.8 PVU) in about 40 h during the intensifying period. Note that the sharp increase in the BPV (i.e., 0.2 PVU in 9 h) coincides well with the amplification of the meridionally averaged PV in the low to midtroposphere during the merging phase (cf. Figs. 5 and 2). Of importance is that about 30% of the increased BPV during this phase is generated by internal dynamics, after taking into account the PV fluxes through the lateral boundaries (i.e., the BPV–mass flux curve in Fig. 5). Note also that the increased BPV rates coincide well to the net mass loss (or pressure falls) in the control volume, which peaks after the merger at 18/21–45. These mass losses imply the possible roles of QCON in determining the time evolution and changes of BPV and TC intensity.

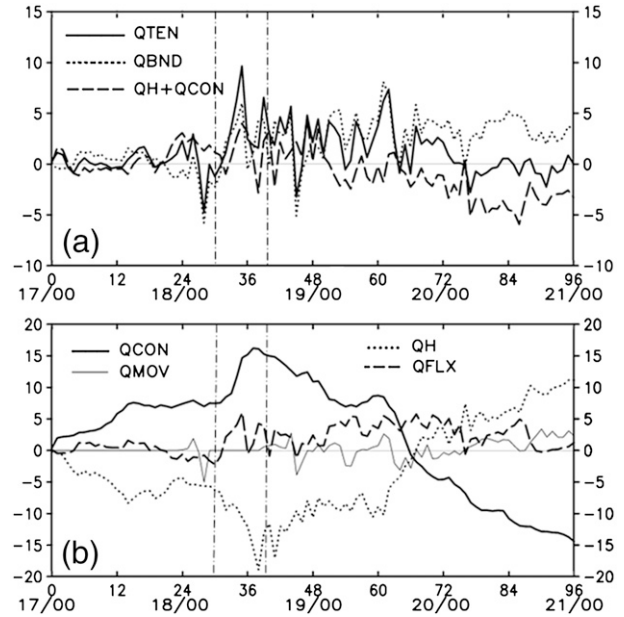


FIG. 6. As in Fig. 5, but for (a) the BPV tendency (solid), the net boundary PV fluxes (dotted), and the sum of the PV condensing and diabatic PV generation rates (dashed); and for (b) the PV condensing rates (solid), the diabatic PV generation rates (dashed), the net PV boundary flux divergence due to normal flows (dotted), and the movement of the control volume (thin solid). The unit is $10^{-6} \text{ PVU s}^{-1}$.

Because the BPV time series can describe well the genesis and dissipation of Eugene, it is desirable to quantify the contributions of different forcing terms on the rhs of Eq. (3) to the time rates of the BPV changes. First, it is necessary to understand the contributions of the net boundary PV fluxes (i.e., QBND) due to the advection of VHTs and meso- γ vortices in the ITCZ, mostly through the western boundary (see Figs. 2–4). Figure 6b shows that pronounced inward PV fluxes (QFLX) into the control volume take place at all times, with a jump occurring between 18/06–30 and 18/12–36 as V_1 moves continuously into V_2 ’s circulation (see Fig. 4). Because of the intermittency of vortices at different scales entering the control volume, QFLX (and QTEN) exhibits marked fluctuations. In contrast, the PV fluxes due to the movement of the control volume (QMOV) are relatively small and vary smoothly with time. Thus, in general, the net PV boundary fluxes (i.e., QBND = QFLX + QMOV) contribute positively to the intensification of Eugene because of the inward fluxes of vortices in the ITCZ, even during the decaying phase (Fig. 6a). Despite such continuous contributions of the PV fluxes to QTEN, the BPV decreases slowly after 20/00–72, suggesting that some internal dynamical processes may determine the weakening of Eugene.

We can see from Eq. (3) that the internal dynamical processes are represented by the first two terms on the rhs: QCON and QH, which are similar in magnitude but opposite in sign (Fig. 6b). That is, QCON is a net source (sink) when the mass in the control volume decreases (increases) (cf. Figs. 6b and 5), whereas QH is a net sink (source) during the intensifying (weakening) stage (cf. Figs. 6b and 7). The time series of QH looks somewhat noisier than that of QCON because of the large variability in diabatic heating gradients associated with deep convection within the ITCZ. Of interest is that QCON contributes positively to QTEN from the early development to the maximum intensity of Eugene near 19/18–66, after which time it switches to a negative sign. In particular, QCON exhibits a sharp increase as V_1 rolls up northwestward and congregates PV patches within V_2 during the merging phase. This sharp increase implies the rapid increase of 3D divergence that results from the expansion of air parcels as they ascend in the intensifying vortex circulation in which the motion is mostly upward. This is consistent with the rapid mass loss and the increased condensing rate of BPV during the merging phase (cf. Figs. 6b and 5). Similarly, the more negative contribution of QCON after 19/18–66 is closely associated with the increased mass gain or the dilution of BPV in the control volume during the decaying stage.

By comparison, the forcing term QH associated directly with diabatic heating shows the time rates of changes that are opposite to QCON, that is, with negative contributions during the early and intensifying periods and positive contributions at the decaying stage (i.e., after 19/18–66), during which stratiform rainfall with an upper-level heating maximum tends to dominate. Such negative contributions of QH to QTEN during the intensifying stage appear at first to contradict our common intuition. This issue could be understood by decomposing QH into its vertical and horizontal components during the three different phases (see Fig. 7). For example, the horizontal part of QH [i.e., $QH_{xy} = (\omega_{xy} \times \nabla_h H)/\rho$, where ω_{xy} and $\nabla_h H$ are the horizontal component of relative vorticity and heating gradients, respectively], often neglected in previous studies, turns out to be very significant and is mostly negative in the vertical (see Figs. 7d–f). Specifically, consider the asymmetric distribution of ω_{xy} and $\nabla_h H$ during the genesis stage due to the fact that diabatic heating occurs mostly in the eastern portion of the control volume (Fig. 2). This tends to generate positive horizontal vorticity (i.e., ω_{xy} points outward when viewed in the cylindrical coordinate) and negative horizontal heating gradients in the eastern half volume and opposite signs in the western half volume in the low to midtroposphere. In contrast, the vertical part of QH [i.e., $QH_z = (\eta \partial H / \partial z) / \rho$, where η

is the vertical component of absolute vorticity] is relatively easier to visualize for the given vertical profiles of H and η (see Figs. 7a–c). That is, QH_z exhibits positive (negative) contributions below (above) the peak heating level, with larger magnitudes in the PBL and near $z = 5$ km where the melting level is located. Because air density decreases exponentially with height, a skewed vertical distribution of $(\eta \partial H / \partial z) / \rho$ would result, with comparable magnitudes aloft despite the presence of small η ; similarly for the vertical distribution of $QH_{xy} = (\omega_{xy} \times \nabla_h H) / \rho$. Summing up the vertical and horizontal parts of QH gives the diabatic PV destruction in most portions of the troposphere during the genesis stage except in the PBL and near the melting level because of the large positive contributions of $(\eta \partial H / \partial z) / \rho$. This is consistent with the net (volume averaged) negative QH contributions to QTEN until Eugene reaches its maximum intensity at 19/18–66 (cf. Figs. 7h, 6b, and 1b).

During the decaying stage (see Figs. 7c,f), the vertical component of QH tends to dominate its horizontal part, mostly because of the decreasing tangential winds and increasing ratio of $(\partial H / \partial z) / \nabla_h H$. Thus, QH switches to a positive sign in the deep troposphere, whereas QCON becomes negative after reaching the maximum intensity (cf. Figs. 7i and 6b). Note that at its early decaying stage, Eugene has well-defined rotational structures but with the peak absolute vorticity located near $z = 5$ km (Fig. 7f). This indicates that the tangential flow increases from the surface to midlevel and then decreases above, implying that ω_{xy} points inward below $z = 5$ km and outward aloft from the vortex center. Despite the large magnitude of ω_{xy} associated with the strong rotation, the contribution of QH_{xy} to QH is small because of the substantial decreases in diabatic heating after 20/00–72 (cf. Figs. 7c,f,i).

Because QH and QCON are ultimately related to diabatic heating, they should be treated as one net forcing in the BPV budget. One can see from Fig. 6a that on average the net forcing (QCON + QH) contributes positively to QTEN prior to 19/03–51 but negatively afterward. Clearly, the storm could still experience a further deepening period [i.e., from 19/03–51 to 19/18–66 (cf. Figs. 6a and 1b)] because of the continued supply of high-PV patches from the ITCZ through the western boundary of the control volume. This implies that without the contribution of QBND, Eugene would likely become much shorter lived under the influence of intense vertical wind shear (see Part I) and with the reducing surface heat fluxes (see Fig. 1b). Subsequently, the destructive effects of QCON due to the dilution of BPV are more or less balanced by the positive contributions of QBND and QH, thereby keeping the BPV tendency nearly null during the decaying stage (cf. Figs. 5 and 6a,b).

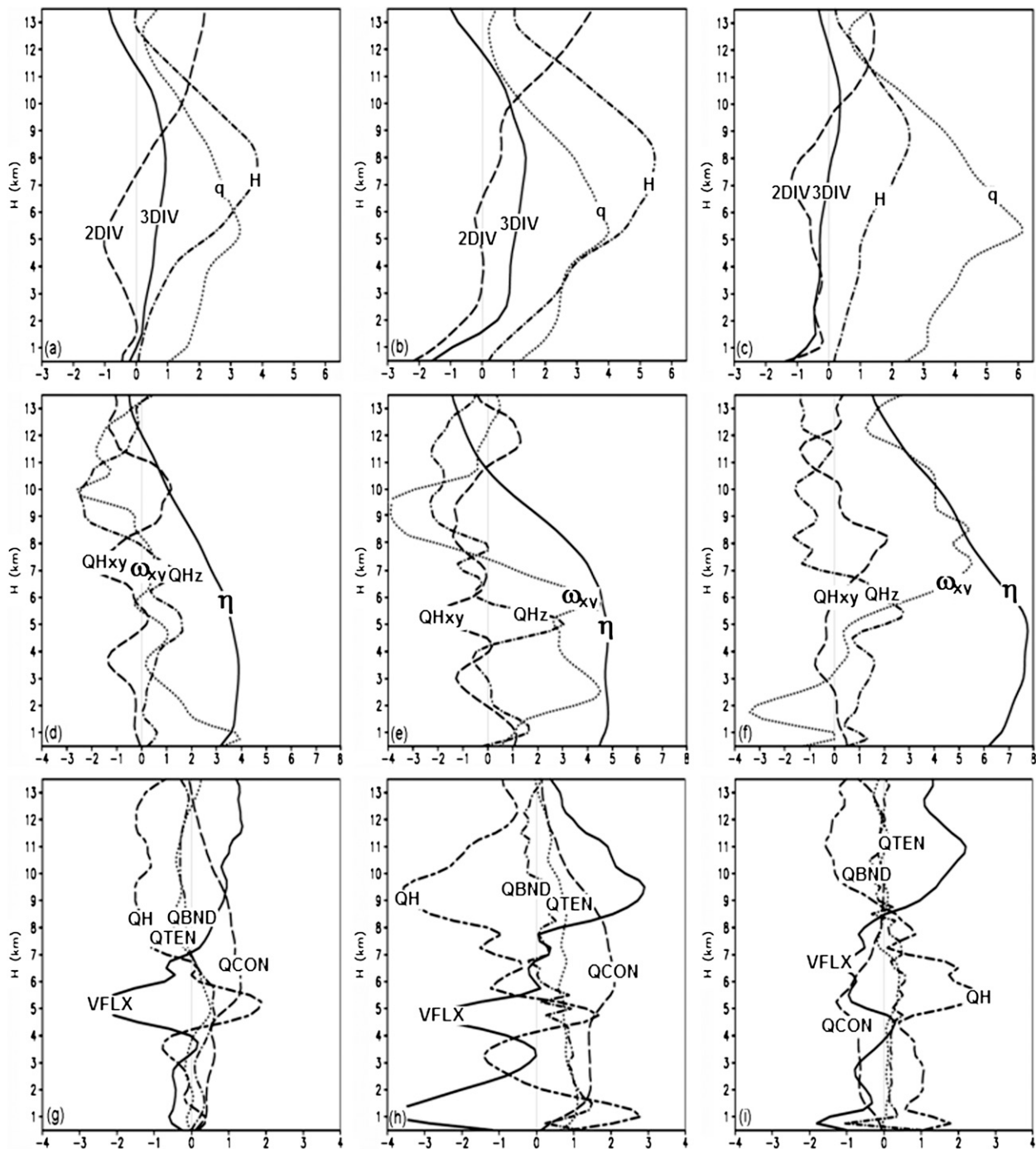


FIG. 7. Vertical profiles of the control (720 km \times 720 km) area-averaged quantities. (top) PV (q ; dotted; 0.2 PVU), 3D velocity divergence (3DIV; solid; 10^{-5} s^{-1}), diabatic heating rates (H ; dotted-dashed; $2 \times 10^{-4} \text{ K s}^{-1}$), and horizontal divergence (2DIV; dashed; 10^{-5} s^{-1}). (middle) The vertical (η ; solid; 10^{-5} s^{-1}) and horizontal (ω_{xy} ; dotted; $5 \times 10^{-4} \text{ s}^{-1}$) components of the absolute vorticity and the vertical (Q_z ; dashed) and horizontal (Q_{xy} ; dotted-dashed) contributions of QH. (bottom) QH (short-long dashed), QCON (dashed), the net boundary PV flux divergence (QBND; dotted-dashed), vertical PV flux divergence (VFLX; i.e., $\partial wq/\partial z$, solid), and QTEN (dotted). All the PV forcing terms have the unit of $10^{-5} \text{ PVU s}^{-1}$. The left, middle, and right columns are for 18/03–27, 18/12–36, and 20/00–72, respectively.

It is important to note that unlike their volume-averaged counterparts, the area-averaged QCON and QH do not cancel out at individual levels, showing significant differences in their vertical structures (Fig. 7). For instance, QH flips signs above and below the melting level during the intensifying stage, whereas QCON remains positive throughout the troposphere with its peak located slightly above the melting level (see Figs. 7g,h). Thus, it is necessary to consider QH and QCON separately when the vertical distribution of the APV budget is examined. Figures 7g–i show that the residues between QCON and QH are more or less balanced at each level by the vertical APV flux divergence included in QBND (i.e., $\partial wq/\partial z$, where w is the vertical motion in height coordinates), which accounts for the vertical transport of APV. Evidently, the vertical APV flux divergence is negative (positive) below (above) the peak APV and vertical motion level, which is opposite in sign but similar in magnitude to the sum of QCON and QH. The net result is that the storm-scale PV increases slowly only in a shallow layer near the melting level prior to merger and during the decaying stage (Figs. 7g and 7i) but at larger rates in the deep troposphere, with the peak magnitude near the top of the PBL during the merging phase (Fig. 7h). The latter result is significant for validating the previously mentioned top-down versus bottom-up hypothesis in the case of vortex merger, namely, the storm-scale positive PV tendency (QTEN) during the merging phase tends to be greater in the lower troposphere rather than at the midlevel. Of interest is that the vertical distribution of QTEN in the lowest 7 km coincides well with that of QBND during most phases, including their peaks near the top of the PBL (see Figs. 7g–i), indicating further the positive roles of CGVs within the two MCVs in the genesis of Eugene. The continued midlevel positive APV tendency during the intensifying phase is consistent with the development of the peak APV near the melting level, for instance, from 0.6 PVU at 18/03–27 to 0.8 PVU at 18/12–36 and 1.2 PVU at 20/00–72 (cf. Figs. 7a–c).

c. Vortex-merging PV dynamics

To see how representative the vertical distributions of the abovementioned area-averaged PV budgets at the three selected times are, Fig. 8 shows the height–time cross sections of APV, potential temperature perturbation (θ') with respect to the initial vertical profile, and 3D divergence, superimposed by the APV forcing terms on the rhs of Eq. (3). First, the storm-scale PV keeps increasing in the deep troposphere, coinciding with the positive forcing of QCON (but mostly negative forcing of QH), until shortly after the decaying stage begins. As mentioned before, the peak APV amplitudes always

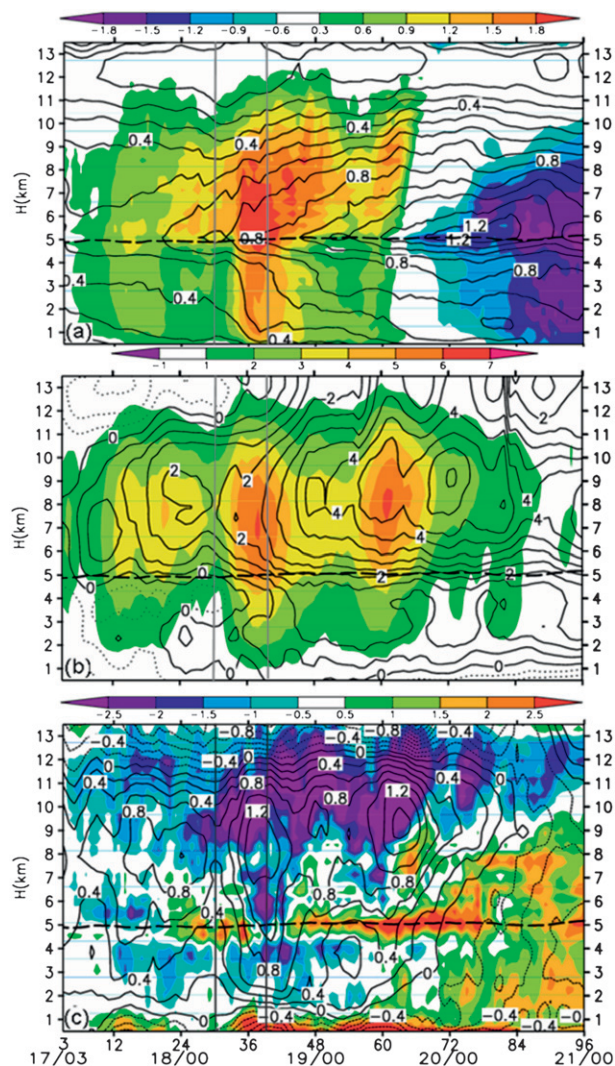


FIG. 8. Height–time cross sections of the control (720 km \times 720 km) area-averaged quantities from the hourly model outputs: (a) PV (solid; every 0.1 PVU) and PV condensing rates (shading; at intervals of 0.3×10^{-5} PVU s^{-1}); (b) diabatic heating rates (shading; at intervals of 0.2×10^{-3} K s^{-1}) and the potential temperature deviation from its initial value (solid; every 0.5 K); and (c) 3D velocity divergence (solid; every 0.2×10^{-5} s^{-1}) and QH (shadings; at intervals of 10^{-5} PVU s^{-1}). Thick dashed lines denote the melting level.

remain slightly above the melting level (i.e., $z = 5$ km) with large vertical gradients below (Fig. 8a). All the other variables (e.g., H , QH, 3DIV, and θ') also exhibit larger vertical gradients in the vicinity of the melting level. This is because the melting cooling below and freezing warming above tend to produce locally large vertical gradients in heating rates (H) and the net warming (θ') profiles; this in turn increases QH through $(\eta \partial H / \partial z) / \rho$, as has also been shown in Fig. 7, assisting partly in the growth of the storm-scale PV above the

melting level. Such larger vertical gradients also appear in the density-decreasing rates (3DIV) and APV condensing rates through QCON (Figs. 8b,c). All these indicate the important roles of melting and freezing in affecting the vertical structures of APV, diabatic heating, and mass convergence during TCG and the life cycle of TCs.

Of relevance to the merging dynamics is the substantial APV increases in the lower troposphere during the merging phase (i.e., with higher APV extending downward to the PBL). This is consistent with the positive PV tendency in both the volume- and area-averaged sense (cf. Figs. 6 and 7e). As shown earlier, the low-level APV increases could be attributed mostly to the congregating CGVs at different scales in V_2 and the subsequent decreases in air density as indicated by QCON (cf. Figs. 2–4, and 8a,c) and partly to the positive contributions of QH in the PBL through $(\eta\partial H/\partial z)/\rho$ (cf. Figs. 8b,c and 7e). In other words, most of the lower-level increases of APV are not the “downward growth” of the midlevel APV associated with the merging MCVs but are caused by the decreasing air mass associated with the advectively collected PV substance (i.e., ρq) within the same isentropic layers.

4. Vorticity dynamics of vortex merger

The bottom-up and top-down hypotheses of TCG associated with MCVs, discussed by Zhang and Bao (1996b), Bister and Emanuel (1997), Ritchie and Holland (1997), and Hendricks et al. (2004), are mainly based on the vorticity dynamics, which could not be easily derived from the PV budgets presented in the preceding section. Thus, in this section, we examine the budgets of the vertical absolute vorticity η to determine which of the above mechanisms is operative in the present vortex merger case.

The time–height cross section of the control-area averaged η (AAV), given in Fig. 9a, shows the presence of larger cyclonic vorticity (about $3 \times 10^{-5} \text{ s}^{-1}$) below the melting level associated with V_2 and slow vorticity growth during the pregenesis phase, and significant vorticity growth during the merging phase, followed by continuous slow amplification until reaching the maximum vorticity of greater than $7.5 \times 10^{-5} \text{ s}^{-1}$ near 20/00–72. Like the APV structure, AAV isopleths also become upright from the peak AAV level down to the surface during the merging phase. However, this AAV isopleth structure could not tell us whether or not such AAV growth occurs from the top downward or the bottom upward. Thus, the local AAV tendency is provided in Fig. 9c, which shows that the vorticity growth does take place in the deep troposphere during the merging phase, but *the most rapid rate appears in the PBL* because of the important con-

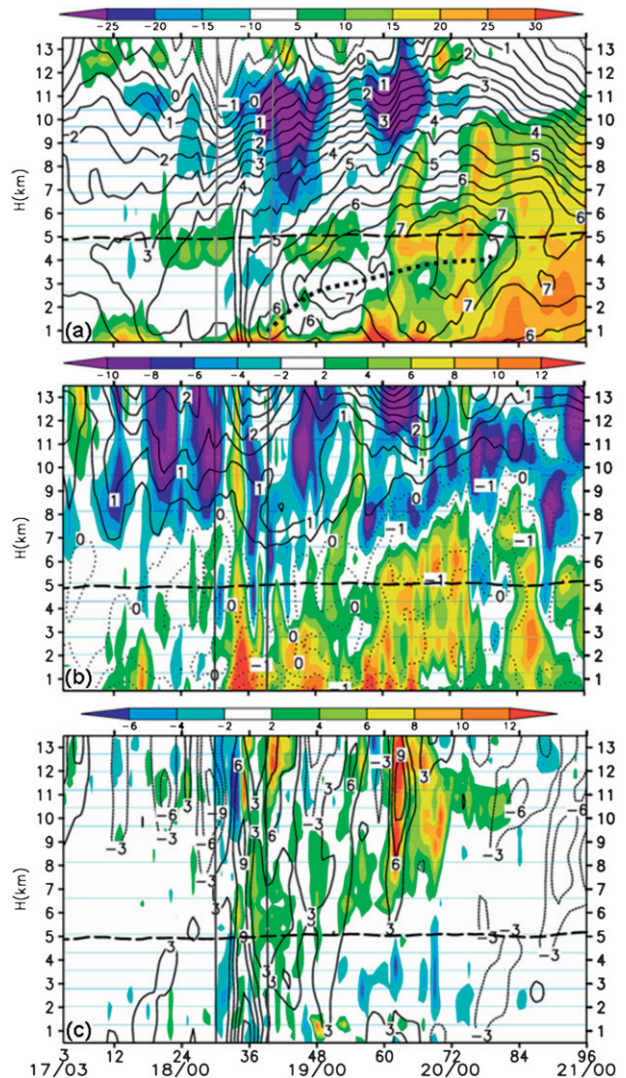


FIG. 9. As in Fig. 8, but for (a) the vertical absolute vorticity (η , every 10^{-5} s^{-1}) and the stretching rates (shaded at intervals of $5 \times 10^{-10} \text{ s}^{-2}$); (b) the bulk stretching rates (shaded at intervals of 10^{-10} s^{-2}) and horizontal divergence (contoured at every 10^{-5} s^{-1}); and (c) the bulk tilting rates (shaded at intervals of 10^{-10} s^{-2}) and the absolute vorticity tendency (solid; every $3 \times 10^{-10} \text{ s}^{-2}$). Bold dashed lines in (a) are for the ridge axis of the absolute vorticity.

tribution of stretching associated with the frictional convergence (Figs. 9a,c). In general, the local vortex stretching has a secondary maximum at the melting level where midlevel convergence is pronounced, but this secondary maximum appears to be insignificant during the merging phase, likely due to the more dominant condensational heating than possible cooling associated with melting. Of interest is that the peak absolute vorticity, growing with time, is elevated from the PBL at the time of merging to a layer near the melting level at 20/00–72.

Unlike in Zhang and Bao (1996b), the peak η could not be maintained near the top of the PBL because of the negative impact of the vertical shear-induced moist downdrafts on the mass convergence in the PBL (see Fig. 14 in Part I).

Because the time evolution of the local AAV tendency, shown in Fig. 9c, consists of several forcing terms including the differential stretching and tilting, 3D advection, and external vorticity flux divergence through the lateral boundaries in a storm-relative reference, it is more meaningful to calculate the η budgets in flux form following Haynes and McIntyre (1987); that is,

$$\begin{aligned} \frac{\partial \eta}{\partial t} &= -\frac{\partial}{\partial x} \left(u\eta + w \frac{\partial v}{\partial z} - F_y \right) - \frac{\partial}{\partial y} \left(v\eta - \frac{\partial u}{\partial z} + F_x \right) + \text{SOL} \\ &= -\left[\frac{\partial(u\eta)}{\partial x} + \frac{\partial(v\eta)}{\partial y} \right] - \left[\frac{\partial}{\partial x} \left(w \frac{\partial v}{\partial z} \right) - \frac{\partial}{\partial y} \left(w \frac{\partial u}{\partial z} \right) \right] \\ &\quad + \left[\frac{\partial F_y}{\partial x} - \frac{\partial F_x}{\partial y} \right] + \text{SOL}, \end{aligned} \quad (4)$$

where the rhs terms of Eq. (4), upon taking area integration and averaging, represent the flux divergence of vorticity forcing through the lateral boundaries, which may be viewed as the lateral η -flux divergence, the divergence of vertically tilted horizontal vorticity, and the frictional and solenoidal contributions, respectively, to the rates of changes of the absolute circulation over the control area. Because the last two rhs terms appear to be much smaller than the first two terms except in the PBL, they are ignored for the purpose of our vorticity budget analysis.

Figure 9b shows that the elevation of the peak η with time could be attributed mainly to the lateral η -flux convergence in the presence of horizontal velocity convergence growing in depth below the heating maxima. Like the vertical stretching structure in Fig. 9a, the lateral η -flux convergence is also peaked in the PBL with a secondary maximum near the melting level; however, on average it grows smoothly in depth with time, as does the horizontal velocity convergence (Fig. 9b), as the storm-scale precipitation evolves from convective to more stratiform (cf. Figs. 7a–c). Again, the most significant features appear during the merging phase; it is dominated by the pronounced lateral flux convergence in the deep troposphere with the maximum rate occurring at the surface (cf. Figs. 9a,b). *This deep layer η -flux convergence could be clearly attributed to the rapid increase in diabatic heating during this phase* (cf. Figs. 9 and 8b). This result conforms to the vertical structures of the bulk local η tendency (cf. Figs. 9b,c) and further confirms the more rapid growth of cyclonic vorticity in the bottom layers. By comparison, the di-

vergence of vertically tilted horizontal vorticity generally contributes much less to the AAV tendency, except at the merging stage (i.e., 18/10–34) and peak intensity (19/15–63), during which it accounts for the significant cyclonic tendencies in the upper troposphere due to the development of strong upward motion and larger vertical wind shear aloft (Fig. 9c).

To gain further insight into the vorticity dynamics during the merging phase, Fig. 10 shows how the vertical structures of the absolute vorticity η evolve at 2-h intervals as the two MCVs approach and then merge to form TS Eugene. The η structures prior to merger are featured with a midlevel high-vorticity volume associated with V_1 and a loosely defined V_2 (cf. Figs. 10a,b and 3). As shown in Part I, V_1 intensifies at the expense of V_2 through enhanced deep convection, leading to the development of a surface mesolow associated with V_1 (see Fig. 10 in Part I). As a result, the frictional and convectively induced horizontal convergence begins to generate cyclonic vorticity in the PBL, and the enhanced divergence above tends to weaken the cyclonic vorticity of V_1 centered at $z = 7$ km. Thus, the largest positive local η tendencies first appear in the bottom layers (Fig. 10a) and then extend upward during the merging and intensifying period (Figs. 10b–f). Again, there is little evidence of the η growth tendency from the midlevel downward. The depth of positive η tendencies grows with time and reaches $z = 10$ km, which is consistent with intense convective developments in the eastern half of the storm circulation (cf. Fig. 10 in Part I and Fig. 10f herein). Similarly, the intensifying cyclonic vorticity begins from the top of the PBL (Fig. 10a) and extends to a deeper layer with time (Figs. 10b–f); there is little physical connection between the lower-level η growth and the midlevel MCVs until the merger is completed. Clearly, this bottom-up η growth contradicts the top-down η -growth hypothesis of Ritchie and Holland (1997) during the MCVs merging phase.

In contrast, negative η tendencies occur in a layer (i.e., $z = 4 \approx 14$ km) in the mid- to upper troposphere that is much deeper than that of the positive η tendencies. This explains why the midlevel cyclonic vorticity weakens because of the presence of strong horizontal divergence during the initial merging stage (Figs. 10a–c) and then appears to intensify slowly because of the upward vorticity advection in the presence of strong updrafts. Nevertheless, the vertical distribution of shallow-layer positive η tendencies below a deep-layer negative η tendency accounts for the generation of a well-defined deep mesoscale vorticity field with the peak intensity near the top of the PBL (Figs. 10e,f). The vertical cross-sectional η structures, shown in Fig. 10f, are similar to those obtained by Zhang and Bao (1996b).

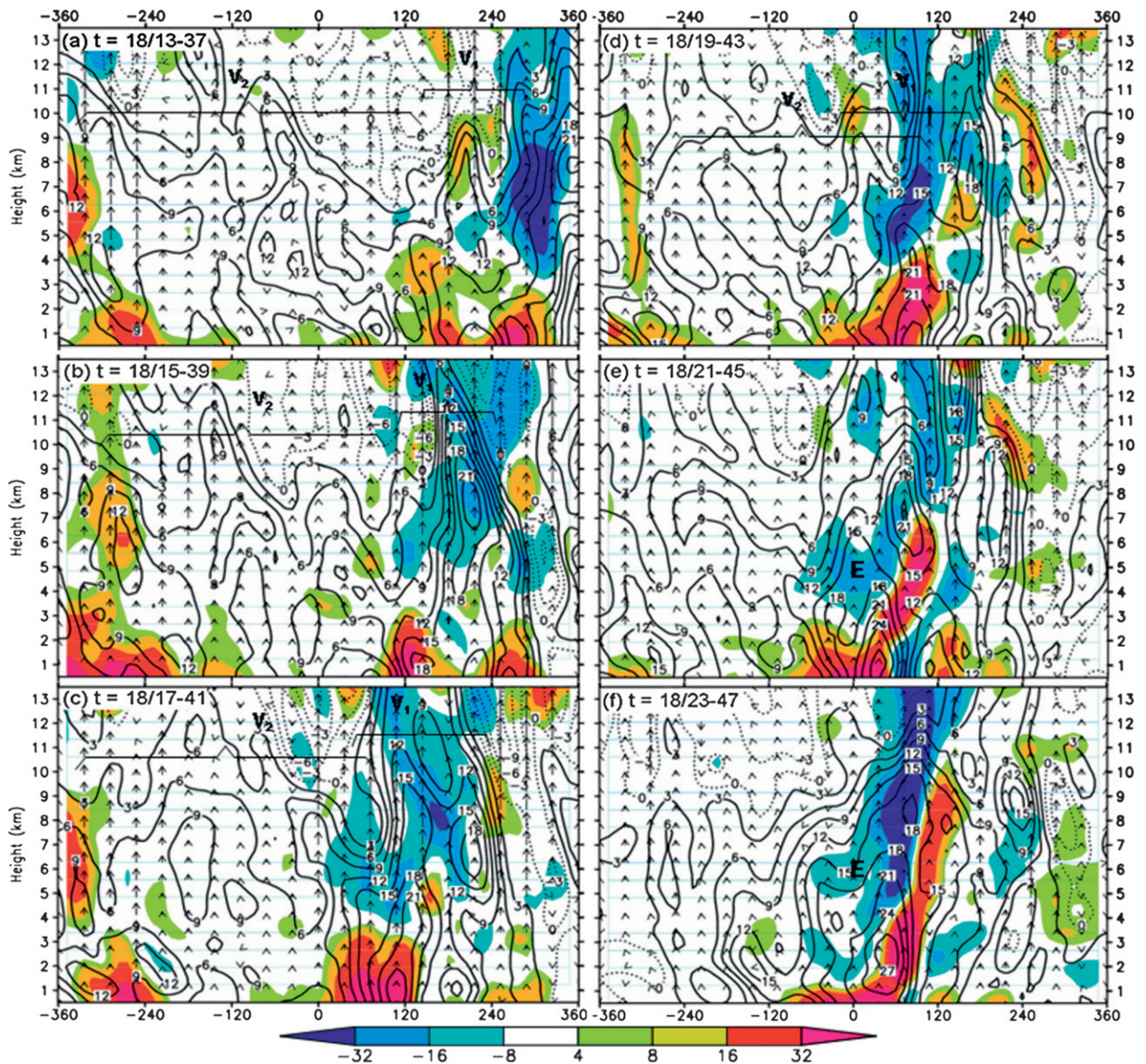


FIG. 10. As in Fig. 2, but for the vertical absolute vorticity (η ; every $3 \times 10^{-5} \text{ s}^{-1}$) superimposed with its total tendency (shaded at intervals of $4 \times 10^{-9} \text{ s}^{-2}$) during the period of 18/13–37 to 18/23–47. Solid (dashed) lines are for positive (negative) values.

Of further relevance to this study is that unlike PV, *the vortex merger does not ensure an increase of the midlevel absolute vorticity* (cf. Figs. 2 and 10) because it cannot adiabatically lead to the midlevel convergence or to any other positive vorticity forcing. In fact, Fig. 9a exhibits near-vanishing to negative net stretching of the absolute vorticity between the melting level and the PBL during the merging phase. This confirms further that the downward growth of cyclonic vorticity would be unlikely to occur either adiabatically or diabatically during the merging phase. However, as shown in Part I, the maximum tangential winds at the rim of the merger, which are the global measures of TC rotation, are shifting

downward as if the storm circulation is developing from the top downward (see Fig. 11 therein). This is because the storm-scale tangential winds tend to spin up rapidly in the PBL as a result of the axisymmetrization of cyclonic vorticity, whereas there are few changes at the midlevel. This top-down evolution of the rotational flows is a manifestation of the bottom-up development of storm-scale cyclonic circulation. Obviously, in the absence of deep convection, even when two MCVs are perfectly superposed in the vertical, stronger horizontal convergence would likely take place in the PBL where larger surface pressure falls occur with cross-isobaric flows, and the cyclonic vorticity would grow first in the

PBL. The merged midlevel flows would still remain rotational with little cross-isobaric (convergent) component.

It should be noted that the η growth in the PBL and midlevel MCVs or peak APV are all indirectly related through the dynamical balance. Specifically, as a deep layer (i.e., from the PBL to the peak heating level) of APV increases in magnitude during the intensifying stage (Fig. 8a), both the mass and wind fields will adjust to the increased PV according to the invertibility principle (Hoskins et al. 1985). This adjustment takes place throughout the vertical columns, but with the maximum downward deformation of isobaric surfaces at the lowest levels, especially in the presence of a warm core from the low to upper layers (Fig. 8b). This is consistent with the more rapid central pressure falls during the merging phase (Fig. 1b herein and Fig. 10 in Part I). Based on the quasi-balanced PV–omega equations system (e.g., Wang and Zhang 2003), we may expect the low-level convergence induced by friction and latent heating to generate cyclonic vorticity in the bottom layer first. Because the η growth through vortex stretching is exponential, especially in the presence of intense updrafts at the MCV scale, the intensifying absolute vorticity would extend upward to form a deep layer of cyclonic rotation. As APV becomes more dominated by its vertical component (i.e., $\eta\partial\theta/\partial z$) during the early weakening stage, the peak absolute vorticity is elevated close to a level (i.e., the melting level) where the peak APV is located (cf. Figs. 7a and 9a). In this case, both η and $\partial\theta/\partial z$ are large below the melting level (see also Figs. 6e,f). In other words, the vertical distribution of APV would differ from that of η when the peak rotation occurs at the lower levels during the intensifying stage because of the important contributions of the horizontal vorticity (see Fig. 6).

5. Summary and concluding remarks

In this study, the genesis of TS Eugene (2005) from merging MCVs is examined using a cloud-resolving simulation with the ARW-WRF at the finest grid resolution of 1.33 km. We have shown in Part I that Eugene originated from the merger of two MCVs associated with the ITCZ breakdowns occurring about 8–9 days earlier. Here the vortex merger is shown in the context of PV not simply as the capture of one MCV (V_1) by another one (V_2) but as the gradual capture of γ -scale CGVs, including VHTs, in the slow-drifting V_2 by the fast-propagating V_1 . Results show that the ITCZ in which V_1 and V_2 are embedded is distributed with many PV patches or CGVs. During the merging phase, V_1 acts as a comma head to roll up and congregate PV-containing CGVs in

V_2 and then in the ITCZ, leading to the concentration of high PV near the center of cyclonic circulation (with its peak amplitude slightly above the melting level) and eventually to the formation of TS Eugene. Of importance is that the low-level PV also increases in magnitude and coverage, resulting from the advection of PV substance associated with the abovementioned CGVs on isentropic surfaces.

The above PV changes are quantified for the life cycle of Eugene through the BPV budget, showing that the bulk PV doubles in magnitude during a 24-h intensifying period, partly because of the net internal dynamical forcing between the BPV condensing and diabatic production and partly because of the continuous PV fluxes from the ITCZ. It is found that surface heat fluxes increase sharply during the merging phase but decrease rapidly shortly after the storm moves to a cold surface. This result indicates that without the PV supply from the ITCZ, the storm would likely be shorter lived under the influence of intense vertical shear and colder sea surface temperatures. Unlike the BPV budget in which the BPV condensing and diabatic production are similar in magnitude but opposite in sign, the APV budget shows quite different vertical distributions between the two forcing terms, which are more or less balanced by the vertical and horizontal APV flux divergence. Results show that the melting and freezing appear to markedly affect the vertical structures of diabatic heating, 3D divergence, mass convergence, vertical vorticity, and APV and its production during TCG and the life cycle of TCs. Results also show the significant horizontal contributions to APV and its production due to the presence of horizontal vorticity that is 30–40 times greater than the vertical absolute vorticity.

It is shown that the vertical absolute vorticity η exhibits initially midlevel maxima associated with the two MCVs, followed by the rapid growth of cyclonic vorticity in the PBL during the merging phase and the subsequent elevation of the peak vorticity to a level close to the melting level at the early decaying phase. The latter could be attributed to the pronounced storm-scale flux convergence of cyclonic vorticity in the presence of horizontal velocity convergence growing in depth below the heating maxima. The bulk η budget reveals that the vorticity growth occurs in the deep troposphere during the merging phase, but the most rapid rate appears in the bottom layers due to the important contribution of the frictional convergence. Of particular importance is that unlike PV, the vortex merger does not show an evident increase of the midlevel cyclonic vorticity because of little midlevel convergence. Thus, we conclude that TCG from merging MCVs would occur from the bottom upward, which is

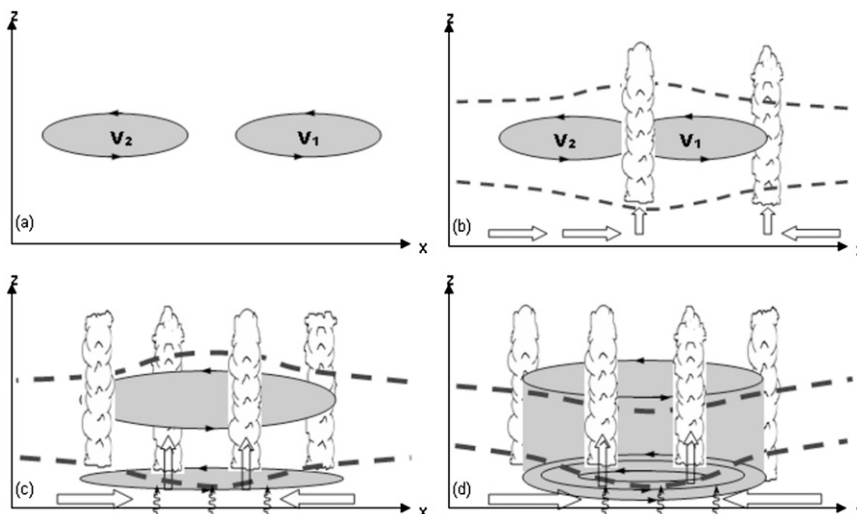


FIG. 11. A schematic description of tropical cyclogenesis from two merging MCVs: (a) prior to merger, (b) during the initial merging phase, (c) complete merging of the midlevel MCVs, and (d) the formation of a tropical storm. The shaded areas with thin arrows denote MCVs; dashed lines show isobaric or isentropic surfaces; wavy arrows denote the surface fluxes; large shaded arrows represent lower-level flow directions.

opposite to the previously hypothesized top-down scenarios. Although this conclusion is obtained from a single case study, we believe that the bottom-up mechanism is applicable to other TCG cases originating from midlevel MCVs. It is worth mentioning that whereas the cyclonic vorticity grows from the PBL upward, the resulting storm-scale rotational flows appear to develop from the midlevel downward, as discussed in Part I.

Based on the above results and those presented in Part I, the genesis of Eugene from the merging MCVs could be conceptualized by Fig. 11 as follows: Assuming that the two MCVs with midlevel warm anomalies approach each other under different environmental flows, both the isentropic and isobaric surfaces will be bowl-shaped below and upward-deformed above, forming a midlevel mesolow at a larger scale (cf. Figs. 11a,b and 2–4 herein and Figs. 4, 6, 10, and 14 in Part I). This mesolow helps reduce pressure below and induce isotropic lifting of high- θ_e air in the low-level southwesterly flows, which facilitates the development of more deep convection in the merger's circulation (cf. Figs. 11b,c herein and Fig. 14 in Part I). The merging phase is characterized by sharp increases in the surface heat fluxes, low-level convergence, latent heating (and upward motion), lower tropospheric PV and cyclonic vorticity growth, and surface pressure falls (see Figs. 1b, 5, 8–10). It is during the merging phase that the WISHE processes are initiated, leading to the rapid growth of surface cyclonic circulations for a self-sustained tropical storm. The storm-scale cyclonic vorticity then grows

from the bottom upward in convective towers distributed in the “eyewall” (cf. Figs. 11c,d, 10e,f, and 3).

Acknowledgments. We are grateful to two anonymous reviewers for their constructive comments that helped improve the presentation of this study. This work was supported by NASA Grant NNG05GR32G and NSF Grant ATM-0758609.

REFERENCES

- Bartels, D. L., and R. A. Maddox, 1991: Midlevel cyclonic vortices generated by mesoscale convective systems. *Mon. Wea. Rev.*, **119**, 104–118.
- Bell, G. D., and D. Keyser, 1993: Shear and curvature vorticity and potential-vorticity interchanges: Interpretation and application to a cutoff cyclone event. *Mon. Wea. Rev.*, **121**, 76–102.
- Bister, M., and K. A. Emanuel, 1997: The genesis of Hurricane Guillermo: TEXMEX analyses and a modeling study. *Mon. Wea. Rev.*, **125**, 2662–2682.
- DeMaria, M., J. A. Knaff, and B. H. Connell, 2001: A tropical cyclone genesis parameter for the tropical Atlantic. *Wea. Forecasting*, **16**, 219–233.
- Emanuel, K. A., 1987: An air–sea interaction model of intraseasonal oscillations in the tropics. *J. Atmos. Sci.*, **44**, 2324–2340.
- Halverson, J., and Coauthors, 2007: NASA's Tropical Cloud Systems and Processes Experiment. *Bull. Amer. Meteor. Soc.*, **88**, 867–882.
- Haynes, P., and M. McIntyre, 1987: On the evolution of vorticity and potential vorticity in the presence of diabatic heating and frictional or other forces. *J. Atmos. Sci.*, **44**, 828–841.
- Hendricks, E. A., M. T. Montgomery, and C. A. Davis, 2004: The role of “vortical” hot towers in the formation of Tropical Cyclone Diana (1984). *J. Atmos. Sci.*, **61**, 1209–1232.

- Hoskins, B. J., M. E. McIntyre, and A. W. Robertson, 1985: On the use and significance of isentropic potential vorticity maps. *Quart. J. Roy. Meteor. Soc.*, **111**, 877–946.
- Kieu, C. Q., and D.-L. Zhang, 2008: Genesis of Tropical Storm Eugene (2005) from merging vortices associated with the ITCZ breakdowns. Part I: Observational and modeling analyses. *J. Atmos. Sci.*, **65**, 3419–3439.
- McBride, J. L., and R. Zehr, 1981: Observational analysis of tropical cyclone formation. Part II: Comparison of non-developing versus developing systems. *J. Atmos. Sci.*, **38**, 1132–1151.
- Molinari, J., D. Volaro, S. Skubis, and M. Dickinson, 2000: Origins and mechanisms of eastern Pacific tropical cyclogenesis: A case study. *Mon. Wea. Rev.*, **128**, 125–139.
- Montgomery, M. T., and R. J. Kallenbach, 1997: A theory for vortex Rossby waves and its application to spiral bands and intensity changes in hurricanes. *Quart. J. Roy. Meteor. Soc.*, **123**, 435–465.
- , and J. Enagonio, 1998: Tropical cyclogenesis via convectively forced vortex Rossby waves in a three-dimensional quasi-geostrophic model. *J. Atmos. Sci.*, **55**, 3176–3207.
- , M. E. Nicholls, T. A. Cram, and A. B. Saunders, 2006: A vortical hot tower route to tropical cyclogenesis. *J. Atmos. Sci.*, **63**, 355–386.
- Nieto Ferreira, R., and W. H. Schubert, 1997: Barotropic aspects of ITCZ breakdown. *J. Atmos. Sci.*, **54**, 261–285.
- Prieto, R., B. D. McNoldy, S. R. Fulton, and W. H. Schubert, 2003: A classification of binary tropical cyclone-like vortex interactions. *Mon. Wea. Rev.*, **131**, 2656–2666.
- Riehl, H., and J. S. Malkus, 1958: On the heat balance in the equatorial trough zone. *Geophysica*, **6**, 503–538.
- Ritchie, E. A., and G. J. Holland, 1997: Scale interactions during the formation of Typhoon Irving. *Mon. Wea. Rev.*, **125**, 1377–1396.
- Simpson, J., E. A. Ritchie, G. J. Holland, J. Halverson, and S. Stewart, 1997: Mesoscale interactions in tropical cyclone genesis. *Mon. Wea. Rev.*, **125**, 2643–2661.
- Wang, C.-C., and G. Magnusdottir, 2006: The ITCZ in the central and eastern Pacific on synoptic time scales. *Mon. Wea. Rev.*, **134**, 1405–1421.
- Wang, X., and D.-L. Zhang, 2003: Potential vorticity diagnosis of a simulated hurricane. Part I: Formulation and quasi-balanced flow. *J. Atmos. Sci.*, **60**, 1593–1607.
- Zhang, D.-L., and J. M. Fritsch, 1987: Numerical simulation of the meso- β scale structure and evolution of the 1977 Johnstown flood. Part II: Inertially stable warm-core vortex and the mesoscale convective complex. *J. Atmos. Sci.*, **44**, 2593–2612.
- , and N. Bao, 1996a: Oceanic cyclogenesis as induced by a mesoscale convective system moving offshore. Part I: A 90-h real-data simulation. *Mon. Wea. Rev.*, **124**, 1449–1469.
- , and —, 1996b: Oceanic cyclogenesis as induced by a mesoscale convective system moving offshore. Part II: Genesis and thermodynamic transformation. *Mon. Wea. Rev.*, **124**, 2206–2226.
- , Y. Liu, and M. K. Yau, 2001: A multiscale numerical study of Hurricane Andrew (1992). Part IV: Unbalanced flows. *Mon. Wea. Rev.*, **129**, 92–107.